1 **Thrusts control the thermal maturity of accreted sediments**

2 Utsav Mannu[1,*], David Fernández-Blanco[2], Ayumu Miyakawa[3], Taras Gerya[4], and Masataka Kinoshita[5]

3 [1]Discipline of Earth Sciences, Indian Institute of Technology, Gandhinagar, India

4 [2]Barcelona Center of Subsurface Imaging, Institut de Ciències del Mar (ICM-CSIC), Barcelona, Spain;

5 [3]Geological Survey of Japan, AIST

6 [4]Institute of Geophysics, ETH Zurich

7 [5]Earthquake Research Institute, UTokyo

8 *Correspondence to*: Utsav Mannu (utsav.mannu@iitgn.ac.in)

9

10

11

12

13

14

15

16

17

18

19

Abstract.

Thermal maturity assessments of hydrocarbon-generation potential and thermal history rarely consider how upper-plate structures developing during subduction influence the trajectories of accreted sediments. Our thermomechanical models of subduction support that thrusts evolving under variable sedimentation rates and décollement strengths fundamentally influence the trajectory, temperature, and thermal maturity of accreting sediments. This is notably true for the frontal thrust, which pervasively partitions sediments along a low and a high maturity path. Our findings imply that interpretations of the distribution of thermal maturity cannot be detached from accounts of the length and frequency of thrusts and their controlling factors. Taking these factors into consideration, our approach provides a robust uncertainty estimate in maximum exposure temperatures as a function of vitrinite reflectance and burial depth thereby reducing former inconsistencies between predicted and factual thermal maturity distributions in accretionary wedges.

51 **1. Introduction**

52 Organic material transforms into coal, oil, and gas at rates primarily controlled by temperature(Quigley & Mackenzie, 1988).

53 This transformation, critical for the hydrocarbon industry, is also useful to study the tectonic and sedimentary evolution of

54 basins and orogens (Tissot et al., 1987; Tissot & Welte, 2013; Waples, 1981). The extent of this transformation in sediments,

55 known as thermal maturity, can be measured as vitrinite reflectance; the percentage of incident light reflected from the surface

56 of vitrinite particles in those sediments (Burnham & Sweeney, 1989). Thermal maturity has been used to estimate the thermal

57 evolution of igneous intrusions(Bostick & Pawlewicz, 1984) and seismic slip(Rabinowitz et al., 2020), the extent of diagenesis

58 and low-grade metamorphism(Ferreiro Mählmann & Le Bayon, 2016; Totten & Blatt, 1993), porosity and compaction in basin

59 sediments (Schmoker & Gautier, 1988), as well as the geothermal history of accreting material during subduction (A.

60 Sakaguchi et al., 2011; Underwood et al., 1992; Yamamoto et al., 2017).

61 Inferences on the geothermal history of subduction margins based on thermal maturity depend on the trajectory

62 followed by the accreting sediments (Miyakawa et al., 2019). Low-temperature high-pressure metamorphic rocks in the

63 subduction wedge are often attributed to the pressure maxima that typically predate the temperature maxima in sediments

64 accreted in the wedge (Platt, 1993). However, numerical models (Ruh, 2020b) and field observations(Giunchi & Ricard, 1999)

65 have indicated the existence of complicated patterns in sediment trajectories. As the orogenic wedge evolves, sediments

66 accreting along different paths reach different depths and velocities and are exposed to different regional peak temperatures.

67 Miyakawa (2019) proposed to subdivide these trajectories based on their final characteristics such as thermal maturity. As a

68 result, the spatiotemporal evolution of the sediments which regulate thermal maturity is controlled, to a first-order, by the

69 partition of incoming sediments along two end-member pathways; (i) a deeper path leading to elevated thermal maturities, the

70 ***high thermal-maturity path***, and (ii) a shallower path resulting in low thermal maturity, the ***low thermal-maturity path***

71 (Miyakawa et al., 2019).

72 Although a number of researchers have studied the diversity of particle paths by their Pressure-Temperature evolution

73 in accreted and underthrusted sediments, in presence of surface processes, distribution of surface processes, in both analytical

74 and numerical models(Hori & Sakaguchi, 2011; Elena Konstantinovskaia & Malavieille, 2005; Platt, 1986; Ruh, 2020a; Wenk

75 & Huhn, 2013), its correlation or lack thereof with its pre-accreted state has not been suitably investigated. Much remains to

3

76   be explored regarding how the partition of high/low thermal maturity paths and the general translation of sediments occurs

77   inside the wedge, given the conventional assumption that accreting sediments remain at the same relative depth (Hori &

78   Sakaguchi, 2011) and translate along the adjacent "layers" without vertical mixing throughout the tectonic evolution of the

79   wedge (Luján et al., 2010; S. Willett et al., 1993) to yield this diversity of sediment paths. To better understand the time-depth

80   paths of wedge sediments, their dependence on the initial state of undeformed sediments, and thus their thermal maturity, the

81   factors that control the evolution of subduction-accretion systems, like sedimentation, erosion, and décollement strength

82   (Mannu et al., 2016; Simpson, 2010), ought to be considered.

83   Here, we explore in detail the impact that a realistic account of accretion in a subduction wedge has on the thermal

84   maturity of its sediments. We simulate subduction-accretion using 2D finite-difference thermomechanical models

85   incorporating empirical thermal conductivity values from the Nankai accretionary margin. We track the evolution of thermal

86   maturity by computing vitrinite reflectance($\%R_0$) using three well-established methods of $\%R_0$ computation, on each marker

87   in the model as the wedge develops by accretion under different sedimentation rates and décollement strengths. These factors

88   notably alter the trajectories and thermal maturities of incoming sediments. Particularly, thrusts define sharp thermal maturity

89   boundaries leading to stark differences in the thermal maturity of sediments that accrete in different thrust blocks, even when

90   they follow similar trajectories and lay nearby.

91

92   **2. Methods**

93   We employ I2VIS, a conservative (Gerya, 2019) finite-difference 2-D thermomechanical subduction-accretion model with

94   visco-plastic/brittle rheology (Gerya & Yuen, 2003). The code solves the governing equations for the conservation of mass,

95   momentum, and heat as well as the advection equation with a non-diffusive marker-in-cell scheme (Gerya, 2019) constrained

96   by thermal conductivity values inferred from Nankai accretionary wedge (Sugihara et al., 2014). Our numerical approach has

97   several advantages over earlier models to simulate thermal maturity in an accretionary wedge(Miyakawa et al., 2019), such as

98   a more realistic geothermal profile, variable particle paths, and thermal evolution. The supplementary material contains

99   information regarding the governing equations, the modified thermal conductivity formulations based on the C0002 borehole

100   in the Nankai accretionary wedge, boundary conditions, the rheological model, model setup (Fig S1) and surface processes(Fig

101   S2).

102   *2.1 An improved thermal maturity calculation*

103   Given that assessments of thermal maturity are inherently reliant on the distribution of temperature inside the wedge, any

104   attempt to model thermal maturity needs a realistic temperature gradient in the wedge. We incorporate this by modifying the

105   thermal conductivity computation for sediments and décollement (see Table 1 and section 1 in the provided supplementary

106   text) to match the empirical relationship between depth and thermal conductivity, as measured on core samples in the borehole

107   IODP Site C0002(Sugihara et al., 2014; Tobin et al., 2015). Both for the same accretionary wedge is scarce to find, and to our

108   knowledge, the C0002 borehole in Nankai accretionary wedge along the Kumano forearc basin is the only place with available

109   datasets for both thermal conductivity and thermal maturity values for an accretionary wedge (Fukuchi et al., 2017). The model

110   computes the $\%R_0$ of each marker to estimate the thermal maturity of sediments during the model run using three widely used

111   methods of thermal maturity modelling Easy$\%R_0$ (Burnham & Sweeney, 1989), Simple$\%R_0$(Suzuki et al., 1993) and Basin$\%R_0$

112   (Nielsen et al., 2017). All these approaches for computing $\%R_0$ yield similar trends albeit different absolute values. In the

113   interest of clarity, we have mostly illustrated Easy$\%R_0$, which is the most extensively used method for Vitrinite Reflectance

114   computation. Hence, in the interest of clarity, we have mostly illustrated Easy%R₀, which is the most extensively used method

115   of Vitrinite Reflectance computation. Hence, hereafter we refer Easy$\%R_0$ as simply $\%R_0$, unless explicitly stated. $\%R_0$ is set

116   to 0.2 in sediment markers at the start of the model till 2.5 Myr, while $\%R_0$ in markers for other rocks, air, and water is

117   undefined at all times. After 2.5 Myr, the model computes $\%R_0$ on each marker as a function of temperature (T), time (t), and

118   amount of fixed carbon as a percentage(f_c). The initial $\%R_0$ of newly deposited sediments is computed using an assumed

119   water-sediment interaction temperature assumed to be the same as the thermocline. The thermocline used in the model has

120   been estimated using the data obtained and made freely available by International Argo Program and the national programs

121   that contribute to it for the region near Nankai (Argo, 2022). is set to 0.2 in sediment markers at the start of the model till 2.5

122   Myr, while %R₀ in markers for other rocks, air, and water is undefined at all times. After 2.5 Myr, the model computes %R₀

123   on each marker as a function of temperature (T), time (t), and amount of fixed carbon as a percentage(f_c). The initial %R₀ of

124   newly deposited sediments is computed using a water-sediment interaction temperature assumed to be the same as the

125   thermocline. The thermocline used in the model has been estimated using the data obtained and made freely available by

126   International Argo Program and the national programs that contribute to it for the region near Nankai (Fig S3, Argo, 2022).

127   *2.2 Experimental Strategy*

128   Here, we present a total of 10 models that vary in their effective basal friction or their effective sedimentation rate to discern

129   patterns of thermal maturity evolution in wedge sediments. Models $M_0^2, M_0^7, M_0^{12}, M_0^{17}, M_0^{22}$, have no sedimentation and

130   effective internal angle values for the décollement of ϕ_b= 2°, 7°, 12°,17° and 22° respectively. The chosen range of effective

131   decollement strength is well within the range of values postulated by several studies for the Nankai accretionary wedge(Tesei

132   et al., 2015). The rest of the models shown here, $M_{0.1}^{12}, M_{0.3}^{12}, M_{0.5}^{12}, M_{0.7}^{12}$, and $M_{0.9}^{12}$ have a medium-strength décollement and

133   variable effective sedimentation rate ranging from 0.1 to 0.9 mm/yr. Sedimentation occurs only at the trench in all of the

134   models presented in this study from sea to land. With these models, we evaluate the particle trajectory and %R_0 of accreting

135   sediments as a function of décollement strength (M_0^2-M_0^{22}) and sedimentation rate ($M_{0.1}^{12}$-$M_{0.9}^{12}$). To restrict the number of

136   parameters influencing our observations, models have no erosion. Moreover, all models lack surface processes during the

137   first ~2.5 Myr and have sedimentation thereafter. Sediments used in the model have an angle of friction of 30° and a strain-

138   softened value of 20° after a threshold of 0.5-1.5 strain. The coefficient of friction increases linearly between the thresholds.

139   Sedimentation rates are the effective sedimentation rate computed after the model run and are thus not prescribed a priori. This

140   choice ensures that the range of average sedimentation in all our models (0.1-0.9 mm/yr) lies within observed sedimentation

141   rates in our chosen natural equivalent, the Nankai accretionary wedge in the south-western subduction margin of Japan(Korup

142   et al., 2014). Table 2 provides more details about the model run and prescribed sedimentary conditions.

143   **3. Results**

144   Subduction begins at 0.1 Myr as the weak material between continental and oceanic plate fails (see supporting information

145   movies). Continued and sustained accretion of sediments against the deforming continental crust forms the accretionary wedge

146   from the interplate contact landwards. After ~5 Myr, all models develop a distinct wedge in agreement with the critical taper

147   theory(Davis et al., 1983). Taper angles increase systematically as effective basal friction increases from ~2° to ~22° (Fig 1,

148   Table 2, $M_0^2 - M_0^{22}$). Whereas models with a relatively weaker décollement, as M_0^2 (ϕ_b= 2°), have taper slopes of 4.3°±

149   0.3°, models with very strong décollement, as M_0^{22} (ϕ_b= 22°), have slopes as steep as 12.8 ± 1.2°(Table 2). Models without

150   trench sedimentation grow solely by accretion of incoming seafloor sediments, with frequent nucleation of frontal thrusts.

151   Models with weaker décollements develop thrusts that are lengthier and remain active for shorter periods. This is clear when

152   comparing, for models with increasingly strong décollement $M_0^2 - M_0^{22}$, the average distance between first and second

153   frontal thrusts are 15.5 ± 7.0 km, 12.1 ± 3.6 km, 8.8 ± 3.3 km, 8.7 ± 2.1 km and 8.0 ± 1.8 km, respectively. Increasing

154   sedimentation rate also leads to an increase in thrust sheet length from 7.3± 1.1 km in $M_{0.1}^{12}$ to 13.8 ± 7.8 km in $M_{0.9}^{12}$. In

155   models with similar basal friction, models with higher sedimentation rates have lengthier thrust sheets that remain active for

156   longer periods (Table 2). Steeper surface slopes with increased décollement strengths and change in thrush sheet length with

157   sedimentation and décollement strength are well-known effects that have been confirmed by previous numerical (Mannu et

158   al., 2016; Wang & He, 1999) and analytical(Malavieille & Trullenque, 2009; Storti & Mcclay, 1995) models. All the reported

159   values are mean ± Standard Deviation values recorded between 2.5-7.5 Myr in individual models. All models, exhibit a

160   temperature gradient that corresponds well with the temperature profile observed in the boreholes at IODP Site C0002 in the

161   Kumano forearc basin, on top of the Nankai accretionary wedge (Fig. S4).

162   *3.1 Thermal maturity of the wedge*

163   Sediments are more thermally mature in wedges that have a higher sedimentation rate or décollement strength. For example,

164   the mean %R_0 of simulations for wedges with the highest sedimentation ($M_{0.9}^{12}$) is 12% higher (0.75) than in those without

165   sedimentation (M_0^2) (Table 2, Fig 1). Similarly, simulations of wedges with the strongest décollement have the highest mean

166   %R_0 (0.94) of all the simulations presented in this study.

167   Thermal maturity values increase with depth and landward distance from the trench to the forearc high irrespective

168   of the decollement strength, sedimentation rates and method of thermal maturity computation (Fig. 1). As a result, sediments

169   at the core of the wedge consistently reach the highest maturity. The absolute value of %R_0 and the rate at which thermal

170   maturity values increase landward from the trench are larger for wedges with high décollement strength(Fig. 2A). In wedges

171   with the same décollement strength but higher trench sedimentation the rate of thermal maturity increase landward from the

172   trench remain very similar(Fig. 2B). Comparing the values of %R_0 (Fig. 2) along an arbitrary horizon in several models

173   emphasizes this result; the model with the highest décollement strength attains the maximum %R_0 of 1.25, and has the highest

174   rate of landward increase in thermal maturity(Fig. 2A). However, all models with similar décollement strength but different

175   sedimentation do not visibly vary in their rate or magnitude of landward increase in thermal maturity. All models show a

176   decrease in thermal maturity landward of the forearc high, commonly of 0.2 %R_0 . Other interesting observations that we

177   explore below are the increased thermal maturity occurring in the vicinity of thrusts (e.g. Fig 1) and the reversal in sediment

178   maturity around out-of-sequence thrust (e.g. Fig 1) active over longer times visible across several models (Fig 1).

179   The magnitude of %R_0 varies consistently among Easy%R_0, Simple%R_0 and Basin%R_0. On average Easy%R_0 have

180   the smallest values, followed very closely by Basin%R_0(with an average difference of only 0.02). However, Simple%R_0 had

181   the highest average value of thermal maturity being 0.16 and 0.13 higher than Easy%R_0 and Basin%R_0 (Fig 1).

182   *3.2 Sediment trajectory inside the wedge*

183   Sediments follow high-maturity paths in larger proportions in wedges with a higher décollement strength or sedimentation

184   rate. We demonstrate this effect by creating a map of the thermal maturity of sediments at 7.5 Myr of the model run, mapped

185   to their spatial position 5 Myr earlier (at 2.5 My of the model run) (Fig. 3) to analyse the spatial correlation between sediment

186   position (depth and distance) from the trench and thermal maturity. We also show the mean thermal maturity attained by

187   sediments at a given horizontal distance from the trench during this period. The scatter plot shows sharp changes with distance

188   from the trench that relate to changes in sediment trajectory (Fig. 3). The mean thermal maturity is also variable along the

189   horizontal length of the wedge and has a periodicity increasing in distance with higher sedimentation rate but relatively constant

190   with changing basal friction (Fig. 3). Whereas the mean thermal maturity has a short periodicity of ~7.2 km for the model

191   M_0^{12} with no sedimentation rates, the model $M_{0.9}^{12}$ shows the longest periodicity of 21 km. However, for all models with the

192   same no sedimentation M_0^2-M_0^{22} the periodicity remains relatively consistent between the range of 7-8 km.

193   Fig 3 also represents the distribution of trajectories that exist in an accretionary wedge and how these trajectories get

194   impacted under trench sedimentation(a subset of these trajectories can be viewed in the supplementary Fig. S5). Whereas in

195   wedges with weak decollements (M_0^2), none of the shallowest half of incoming sediments reach %R_0 > 1 in 5 Myr, 2% of

196   sediments reach this value in wedges with strong décollement (M_0^{22}). The effects of décollement strength in the thermal

197   maturity of sediments can be quantified as well at deeper levels, with one-eighth vs more than half of the sediments surpassing

198   values of %$R_0 = 1$ for the deepest half of incoming sediments (12.0% and 54% respectively) in weak vs strong-decollement

199   wedges(M_0^2 vsM_0^{22}), respectively. Increasing the sedimentation rate shows this effect even more prominently. In wedges

200   from the model without sedimentation(M_0^{12}), none of the top half m of sediments yield %$R_0 > 1$, while ~ 15% of them surpass

201   %$R_0 > 1$ in the models with a sedimentation rate of 0.9 mm/yr ($M_{0.9}^{12}$). In sum, the proportion of sediments in the top half and

202   bottom half of the wedge that reach high maturity steadily increases with both sedimentation rate and décollement strength

203   (Table 2).

3.3 Patterns of trajectory and thermal maturity in incoming sediments

205   The diversity in the trajectory of sediments in the wedge leads to a plethora of pathways in which the sediments can become

206   thermally mature and thus introduces epistemic uncertainty in the estimation of maximum exposure temperature. Fig 4,

207   captures this uncertainty where we plot the maximum exposure temperature as a function of %R_0 for all the models simulated

208   in this study. We find that almost all the models show a remarkable similarity in their relationship between maximum exposure

209   temperature and %R_0 (for individual models ~~please~~ see Fig S6) and differ mostly in their proportion of sediments with extreme

210   values of %R_0. We observe that the typical uncertainty in maximum exposure temperature increases with an increase in values

211   of %R_0 with ~ 15°C interval at around %R_0=0.2 compared to ~33°C interval at %R_0= 3 (both for 95% confidence interval,

212   Fig. 4b). Furthermore, we observe that information about the present depth of the sediments w.r.t the thickness of the wedge

213   (as represented by different colours in Fig 4a) greatly helps to further constrain the maximum exposure temperature. For

214   instance, although the overall uncertainty at %R_0=1, is ~23°C, for sediments with a normalized depth of 0.2-0.4, the uncertainty

215   greatly reduces to only ~10.5°C. Thus the range of thermal maturity values for sediments clearly has a large correlation with

216   their trajectories.

217 *3.4 Comparision of Easy%R₀ Simple%R₀ and Basin%R₀*

218 Finally as our models produced three sets of %R$_0$ using Easy%R$_0$(referred to as R$_0$% throughout our study-), Simple%R$_0$ and

219 Basin%R$_0$, it also gives us a unique perspective on comparative advantages of each method. Uncertainty for all three models

220 increases with increasing %R$_0$ from ~20–25°C at ~0.3 which rises to ~35°C at R$_0$%=3.5(Fig 4b). Easy%R$_0$ is the most well-

221 recognised method of thermal maturity computation and yields the best constraint on uncertainty for very small changes

222 around the values less than 1. For the values of %R$_0$ between 1 and 3, all models yield very similar uncertainty, with

223 Simple%R$_0$ yielding the most constrained exposure temperatures(Fig 4b). However, beyond R$_0$%=3, the Simple%R$_0$ becomes

224 highly unreliable, with uncertainty in exposure temperatures as high as 55°C at R$_0$%=4. Easy%R$_0$ yields a reasonable

225 uncertainty range of ~37°C till R$_0$%=4.4, but starts to be unreliable above this value. Basin%R$_0$ remains consistent till a very

226 high value of R$_0$%(~6), and thus provides the best constraint on the widest range of values of thermal maturity(Fig 4b).

227

228 **4. Discussion**

229 Our models achieve realistic thermal maturity distributions thanks to unique computational advantages over models in the

230 previous studies(Mannu et al., 2016, 2017; Miyakawa et al., 2019), despite several relevant assumptions. Models are simplified

231 by assuming no elasticity, predefined décollement, no erosion, and using simple and uniform rheology, and either has an

232 insufficient resolution or lack empirical relations to simulate the compaction of sediments and processes of multiscale fluid

233 flow. Although these assumptions hinder a wholesale comparison between our simulations and natural examples of

234 accretionary wedges, we are confident of the thermal maturity patterns of our models. Our estimated %R$_0$ values for the model

235 $M_{0.1}^{12} - M_{0.9}^{12}$ are in very good agreement with the %R$_0$ values measured for the borehole C0002 Nankai accretionary wedge

236 (used for thermal conductivity values) by Fukuchi et. al. 2009 (Figure 5). Moreover, the temperature estimated from the

237 observed thermal maturity of a timeframe of 1-2 Myr in the borehole, also strongly correlates with the trend and the range of

238 95% Confidence interval of T vs %R$_0$ estimated in our models (Fig S7). Furthermore, our models also correlate with the

239 patterns of P-wave velocity for Nankai(Górszczyk et al., 2019; Nakanishi et al., 2018) and Hikurangi(Arai et al., 2020)

240 margins(Dewing & Sanei, 2009). Models compute realistic thermal maturity distributions thanks to several key improvements.

241 Firstly, our models calculate temperature gradients that evolve at long time intervals and thus closely replicate accretionary

242 wedges in nature (Fig. S2). This enables the simulation of realistic temperature profiles based on thermal conductivity values

243 derived empirically from natural accretionary wedges, as in our case, the Nankai margin(Sugihara et al., 2014) Secondly, our

244 simulations account for the effects that thermal and isostatic feedback from the oceanic lithosphere have on the evolution of

245 the wedge by simulating plate subduction at a large scale rather than just the accretionary wedge(Miyakawa et al., 2019).

246 Finally, our method calculates the vitrinite reflectance of sediments on each marker of the model. This capacity to accurately

247 estimate thermal maturity in each marker informs the research questions of this study and allows inferences beyond those of

248 depth-dependent thermal maturity distributions.

249 The thermal maturity of the wedge increases landward, as signalled by the landward increase in $\%R_0$ (Fig. 1). This

250 has been observed in natural accretionary wedges such as Miura–Boso plate subduction margin (Yamamoto et al., 2017), fold

251 and thrust belts Western Foothills complex in western Taiwan (Arito Sakaguchi et al., 2007) and other numerical models of

252 accretion(Miyakawa et al., 2019), resulting from the long-term deformation of older accreted sediments and the backstop-

253 forced exhumation in the wedge. Our models show that the rate of landward rise in thermal maturity is faster for thicker wedges

254 (Fig 2). This is the case for wedges with high basal strength(M_0^{22}), for sediments in thicker wedges deform more prominently

255 than those in their thinner counterparts. Simulations also show that sediments reach deeper levels in thicker wedges and that

256 this increases the overall thermal maturity of the wedge. Also, increased exhumation rates and steeper thermal maturity

257 gradients occur in the wedge interior, as the continental backstop deflects sediment trajectories upwards during accretion (Fig.

258 2). As a result, for the geometry of the backstop used in our models, backstop-forced exhumed material is, on average,

259 thermally more mature.

260 Our models expose two relevant cases where the increase of thermal maturity with depth or landward is relevantly

261 altered: on-fault increase and fault-block inversion. Our models attest to the steep rise in thermal maturity of sediments at fault

262 sites (Fig. 1). This is well documented in nature, as for boreholes C0004(Sakaguchi et al., 2011). However, on-fault increases

263 in thermal maturity are comparatively smaller in our simulations and lack the marked increase in $\%R_0$ observed at fault sites

264 in nature. This is primarily due to our models developing wider fault zones than their natural equivalents and the subsequent

265 acceleration in the thermal diffusion occurring in simulated thrusts. During fault-block inversions, the positive gradient of

266 thermal maturity with depth is inverted by thrusting relatively mature sediments over less mature sediments(Underwood et al.,

267 1992). This is known from natural observations, as along the Fukase Fault in Shimanto accretionary wedge(Ohmori et al.,

268 1997) and underneath the forearc basin in Nankai accretionary wedge(Fukuchi et al., 2017), and previous modelling

269 efforts(Miyakawa et al., 2019).

270 Collation of the above implies that the thermal maturity of accretionary wedges results from the general increase of

271 thermal maturity (i) with depth and (ii) landward, as well as from its (iii) modification by thrust faults. Our models suggest

272 thermal maturity inversions by thrusting, which are commonplace in accretionary contexts, are the primary cause of thermal

273 maturity differentiation among wedges with initially similar geothermal gradients. In other words, the strong differentiation in

274 the trajectory of sediments led by thrusting has a larger influence over thermal maturity than burial depth or in-wedge location.

275 This novel inference has probably remained concealed thus far due to the large number of parameters that condition thrust

276 development, frequency, length, and thermal state. Influencing parameters to include sedimentation, erosion, basal friction and

277 relief, pore pressure and fluid state, wedge length and thickness, taper angle, and many others(Dominguez et al., 2000; E.

278 Konstantinovskaia, 2005; Mannu et al., 2016; Ruh, 2017; Simpson, 2010; H. J. Tobin & Saffer, 2009). It is nevertheless

279 important to note that the frequency of faults in a wedge can be impacted by many other factors, including hinterland

280 sedimentation(Simpson, 2010; Storti & Mcclay, 1995), erosion(E. Konstantinovskaia, 2005; S. D. Willett, 1999), and seafloor

281 topography(Dominguez et al., 2000). Below, we discuss how thrusts not only alter the thermal evolution of accreting sediments

282 but are, in fact, the primary control of their thermal maturity.

283 Thermal maturity correlates with sediment depth weakly near faults and more strongly away from them. The distance

284 of sediment from frontal thrust dictates the trajectory of sediment grains, and as a result, the pressure-temperature conditions

285 to which they are exposed. In this study, we have considered solely how décollement strength and the rate of trench

286 sedimentation vary the frequency, architecture, and overall behaviour of thrusts, and the frontal thrust, as the wedge evolves.

287 Our results show the need to consider all factors influencing fault frequency when inferring the geothermal history of

288 contractional terrains by means of thermal maturity. Fortunately, this predictive exercise should be relatively straightforward,

289 for the impact of these external factors on the fault structure of wedges has been established(Fillon et al., 2012; Mannu et al.,

290 2016, 2017; Mugnier et al., 1997; Simpson, 2010; Storti & Mcclay, 1995), and the effect of each of these factors can be

291 accounted for when assessing the trajectory of sediments and the distribution of thermal maturity in accretionary wedges.

292   Sediment mixing in subduction wedges is primarily controlled by thrusting. Previous studies have reached seemingly

293 contradicting outcomes when using numerical(Miyakawa et al., 2019; Wenk & Huhn, 2013; S. Willett et al., 1993) and

294 analogue(E. Konstantinovskaia, 2005; Mulugeta & Koyi, 1992) approaches to analyze sediment trajectories as a function of

295 changes in erosion, sedimentation, or décollement strength. While some studies showed that the rate and extent of a transition

296 by which sediment trajectories change from generally horizontal to increasingly vertical during accretion change consistently

297 with the initial depth of incoming sediments(Mulugeta & Koyi, 1992; S. Willett, 1992), others predicted different crossover

298 paths for sediments accreting over a range of décollement strengths(E. Konstantinovskaia, 2005). Our models show that both

299 are valid results and that changes in trajectory patterns leading to path crossovers are controlled by the horizontal distance of

300 sediments from the frontal thrust. Starting at a threshold distance from the trench, sediments at different depths follow laminar

301 paths along different trajectories within the wedge. Laminar-type trajectories can be reproduced in a broad range of simulations

302 and are particularly common in models with low sedimentation and décollement strengths. However, the depth dependence of

303 sedimentary paths varies periodically as a function of distance from the trench of specific sedimentary packages (Fig. 3,6).

304 This effect, which is particularly marked in the neighbourhood of the frontal thrust, explains the crossover paths for incoming

305 sedimentary packages at similar depths and different horizontal locations, as shown by Konstantinovskaia et al. 2005.

306 Therefore, thrust faults in the wedge act as the primary agent controlling whether sediments sustain depth-controlled laminar

307 flow or mix.

308   The thermal maturity that incoming sediments reach varies periodically as a function of thrust frequency. Although

309 previous research considered non-laminar sediment trajectories as chaotic(Mary et al., 2013), and the wide variety of

310 trajectories shown in our models seem to agree with this (Fig 3, Fig S4), patterns emerge when we correlate the lateral and

311 vertical position of incoming sediments with their eventual thermal maturity. Changes in the depth of the thermal maturity

312 boundary are less frequent and have larger amplitudes with increased décollement strength, and especially, increased

313 sedimentation rates (Fig. 4). The periodicity in the thermal maturity boundary marks the periodic oscillation of the predominant

314 trajectory followed by incoming sediments, i.e., between accretion (low thermal maturity path) and underthrusting (high-

315 thermal maturity path). As a result, it should also strongly correlate with the periodicity observed in the evolution of forearc

316 topography(Menant et al., 2020) and the frequency of thrust formation as such in our models. This is expected, given that

317 thrusts are active over longer mean times, and they thus channel material toward the décollement more efficiently, in wedges

318 with stronger décollement or increased sedimentation. While sediments at internal and higher structural positions of the wedge

319 are translated towards the surface and have a lower thermal maturity, sediments at external and lower structural positions are

320 translated towards the décollement and have a relatively higher maturity. This is a relevant observation, for it typifies the

321 causality of particular sediment grains following a high or low maturity path, a long-standing unanswered question(Miyakawa

322 et al., 2019). We corroborate this observation by analyzing the ~~terminal~~ thermal maturity of sediments across a frontal thrust

323 active at a younger age. For example, by showing the thermal maturity of sediments at ~7.5 Myr across a thrust active at ~4

324 Myr, as in Fig. 7. Whereas this occurs for all thrusts in the wedge, the frontal thrust is particularly pronounced in partitioning

325 sediments into the high and low maturity paths.

326 Geothermal information stored in the incoming sediments can only be retrieved if sediments are at appropriate

327 locations with respect to emergent thrusts. We illustrate this using two runs of the same model and tracking an artificial thermal

328 anomaly imposed on incoming sediments at two different locations (Fig. 7). This hypothetical thermal anomaly can be

329 conceptualized as any alteration of the thermal maturity profile of incoming sediments, for example, elevated heat flows by an

330 antecedent magmatic intrusion. While the change in $\%R_0$ associated with the short-lived thermal anomaly results in abnormally

331 high values of thermal maturity in both sediment packages, it can only be retrieved for the end-model run of sediments located

332 further from the trench (those in the right panel, Fig. 7b). Contrarily, the end-model run of sediments closer to the trench (those

333 in the left panel, Fig. 7a) shows no signs of discontinuity in the thermal maturity distribution of the wedge. This is because we

334 deliberately placed the thermal anomaly at sites that evolve at two structural locations during the model run, i.e., above and

335 below a yet-undeveloped frontal thrust (Fig. 7). The sediment sector affected by the thermal anomaly closer to the trench is

336 overthrusted by the frontal thrust and remains in a footwall location thereafter (Fig. 7a). In contrast, the homologous

337 sedimentary package further away from the trench is accreted by the frontal thrust and remains in a hanging-wall location (Fig.

338 7b). Thus, the preservation of the record of an antecedent thermal anomaly is only possible in the former case. We further note

339 that, in our simulations, the entire vertical column of sediments records the thermal anomaly, while in nature, the anomaly may

340   affect only sediments at the deeper locations of the sedimentary pile, which are in turn the sediments that most likely to follow

341   a high-maturity path. We thus regard the possibility of retrieving such antecedent geothermal information as minimal.

342   The main implications of this contribution emerge from its predictive power. Our approach can predict to a precise the thermal

343   maturity of sediments and the uncertainty associated with the maximum exposure temperature in accretionary contexts with

344   known structuration. More accurate quantification of the thermal evolution and thermal state of accreted sediments reduces

345   the uncertainties attached to the location of temperature-led transformations of organic material into hydrocarbons in

346   subduction margins and other accretionary contexts. Such increased accuracy in the distribution of thermally mature sediments

347   may also be applied for improved assessments of the evolution in time of any other geothermal process, including seismic slip,

348   magmatic and metamorphic extent, porosity, compaction and diagenesis of sediments, and the reconstruction of convergent

349   margins in general(Bostick & Pawlewicz, 1984; Ferreiro Mählmann & Le Bayon, 2016; Rabinowitz et al., 2020; A. Sakaguchi

350   et al., 2011; Totten & Blatt, 1993; Underwood et al., 1992).

351   Finally, among the three methods of $\%R_0$ computation, Easy$\%R_0$ and Basin$\%R_0$ are clearly more consistent and well-

352   constrained on a wide range of thermal maturity in comparison to Simple$\%R_0$, which seems to be particularly useful for a

353   smaller range of thermal maturity values. This simply illustrates the fact that while Easy$\%R_0$ and Basin$\%R_0$ computation

354   deals with several parallel reactions related to the maturity of kerogen(and hence multiple activation energies), the Simple$\%R_0$

355   is based on best-fitted single activation energy, and hence yields large confidence intervals at the extreme $\%R_0$ values.

356   Additionally, the inclusion of the higher activation energy reactions in Basin$\%R_0$ makes it the best-suited formulation for

357   sediments at the deeper and shear zone sediments which usually get saturated using Easy$\%R_0$.

358   **4. Conclusion**

359   This study demonstrates how contractional faults alter the paths of sediments as they accrete and how this fundamentally

360   controls the distribution of the thermal maturity of sediments in accretionary wedges and emphasizes the role that

361   sedimentation rate and interplate contact strength have in such distribution. The increased resolution of our approach leads to

362   findings that have relevant implications. For example, the geothermal history that can be retrieved from the thermal maturity

363   of sediments in drills, i.e., at the shallow wedge, provides, at best, an incomplete record that is skewed towards the thermal

364 evolution of sediments near the trench. Coevally, relevant sectors of sediments located further seaward, when not subducted,

365 follow high-maturity paths that overprint their antecedent thermal history. Finally, this study also provides a first-order

366 uncertainty measure for the thermal maturity of sediments based on the diversity in their trajectory.

367 **Competing interests**

368 The authors declare that they have no conflict of interest.

369 **References**

370 Arai, R., Kodaira, S., Henrys, S., Bangs, N., Obana, K., Fujie, G., et al. (2020). Three-dimensional P wave velocity

371 structure of the northern hikurangi margin from the NZ3D experiment: Evidence for fault-bound anisotropy. *Journal of*

372 *Geophysical Research, [Solid Earth]*, *125*(12). https://doi.org/10.1029/2020jb020433

373 Argo. (2022). Argo float data and metadata from Global Data Assembly Centre (Argo GDAC) [Data set]. SEANOE.

374 https://doi.org/10.17882/42182

375 Bostick, N. H., & Pawlewicz, M. J. (1984). Paleotemperatures based on vitrinite reflectance of shales and limestone in

376 igneous dike aureoles in the Upper Cretaceous Pierre shale, Walsenburg, Colorado. Retrieved from

377 http://archives.datapages.com/data/rmag/SourceRocks84/bostick.pdf

378 Burg, J.-P., & Gerya, T. V. (2005). The role of viscous heating in Barrovian metamorphism of collisional orogens:

379 thermomechanical models and application to the Lepontine Dome in the Central Alps. *Journal of Metamorphic*

380 *Geology*, *23*(2), 75–95.

381 Burnham, A. K., & Sweeney, J. J. (1989). A chemical kinetic model of vitrinite maturation and reflectance.

382 *Geochimica et Cosmochimica Acta*, *53*(10), 2649–2657.

383 Byrne, T., & Fisher, D. (1990). Evidence for a weak and overpressured décollement beneath sediment-dominated

384 accretionary prisms. *Journal of Geophysical Research*. https://doi.org/10.1029/jb095ib06p09081

385 Davis, D., Suppe, J., & Dahlen, F. A. (1983). Mechanics of fold-and- thrust belts and accretionary wedges. *Journal of*

386 *Geophysical Research*. https://doi.org/10.1029/JB088iB02p01153

387 Dewing, K., & Sanei, H. (2009). Analysis of large thermal maturity datasets: Examples from the Canadian Arctic

388 Islands. *International Journal of Coal Geology*, *77*(3), 436–448.

389   Dominguez, S., Malavieille, J., & Lallemand, S. E. (2000). Deformation of accretionary wedges in response to

390   seamount subduction: Insights from sandbox experiments. *Tectonics*, *19*(1), 182–196.

391   Ferreiro Mählmann, R., & Le Bayon, R. (2016). Vitrinite and vitrinite like solid bitumen reflectance in thermal

392   maturity studies: Correlations from diagenesis to incipient metamorphism in different geodynamic settings.

393   *International Journal of Coal Geology*, *157*, 52–73.

394   Fillon, C., Huismans, R. S., & van der Beek, P. (2012). Syntectonic sedimentation effects on the growth of fold-and-

395   thrust belts. *Geology*, *41*(1), 83–86.

396   Fukuchi, R., Yamaguchi, A., Yamamoto, Y., & Ashi, J. (2017). Paleothermal structure of the N ankai inner

397   accretionary wedge estimated from vitrinite reflectance of cuttings. *Geochemistry, Geophysics, Geosystems*, *18*(8),

398   3185–3196.

399   Gerya, T. (2019). *Introduction to Numerical Geodynamic Modelling*. Cambridge University Press.

400   Gerya, T. V., & Yuen, D. A. (2003). Characteristics-based marker-in-cell method with conservative finite-differences

401   schemes for modeling geological flows with strongly variable transport properties. *Physics of the Earth and Planetary*

402   *Interiors*, *140*(4), 293–318.

403   Giunchi, C., & Ricard, Y. (1999). High-pressure/low-temperature metamorphism and the dynamics of an accretionary

404   wedge. *Geophysical Journal International*, *136*(3), 620–628.

405   Górszczyk, A., Operto, S., Schenini, L., & Yamada, Y. (2019). Crustal-scale depth imaging via joint full-waveform

406   inversion of ocean-bottom seismometer data and pre-stack depth migration of multichannel seismic data: a case study

407   from the eastern Nankai Trough. *Solid Earth*, *10*(3), 765–784.

408   Hori, T., & Sakaguchi, H. (2011). Mechanism of décollement formation in subduction zones. *Geophysical Journal*

409   *International*, *187*(3), 1089–1100.

410   Konstantinovskaia, E. (2005). Erosion and exhumation in accretionary orogens: Experimental and geological

411   approaches. *Geochemistry, Geophysics, Geosystems*. Retrieved from

412   https://agupubs.onlinelibrary.wiley.com/doi/abs/10.1029/2004GC000794

413   Konstantinovskaia, E., & Malavieille, J. (2005). Erosion and exhumation in accretionary orogens: Experimental and

414   geological approaches. *Geochemistry, Geophysics, Geosystems*. https://doi.org/10.1029/2004gc000794

415   Korup, O., Hayakawa, Y., Codilean, A. T., Matsushi, Y., Saito, H., Oguchi, T., & Matsuzaki, H. (2014). Japan's

416   sediment flux to the Pacific Ocean revisited. *Earth-Science Reviews*, *135*, 1–16.

417   Luján, M., Rossetti, F., Storti, F., Ranalli, G., & A. Socquet. (2010). Flow trajectories in analogue viscous orogenic

418   wedges: Insights on natural orogens. *Tectonophysics*, *484*(1), 119–126.

419   Malavieille, J., & Trullenque, G. (2009). Consequences of continental subduction on forearc basin and accretionary

420   wedge deformation in SE Taiwan: Insights from analogue modeling. *Tectonophysics*, *466*(3), 377–394.

421   Mannu, U., Ueda, K., Willett, S. D., Gerya, T. V., & Strasser, M. (2016). Impact of sedimentation on evolution of

422   accretionary wedges: Insights from high-resolution thermomechanical modeling. *Tectonics*.

423   https://doi.org/10.1002/2016tc004239

424   Mannu, U., Ueda, K., Willett, S. D., Gerya, T. V., & Strasser, M. (2017). Stratigraphic signatures of forearc basin

425   formation mechanisms. *Geochemistry, Geophysics, Geosystems*, *18*(6), 2388–2410.

426   Mary, B. C. L., Maillot, B., & Leroy, Y. M. (2013). Deterministic chaos in frictional wedges revealed by convergence

427   analysis. *International Journal for Numerical and Analytical Methods in Geomechanics*.

428   https://doi.org/10.1002/nag.2177

429   Menant, A., Angiboust, S., Gerya, T., Lacassin, R., Simoes, M., & Grandin, R. (2020). Transient stripping of

430   subducting slabs controls periodic forearc uplift. *Nature Communications*, *11*(1), 1823.

431   Miyakawa, A., Kinoshita, M., Hamada, Y., & Otsubo, M. (2019). Thermal maturity structures in an accretionary wedge

432   by a numerical simulation. *Progress in Earth and Planetary Science*, *6*(1), 8.

433   Mugnier, J. L., Baby, P., Colletta, B., Vinour, P., Bale, P., & Leturmy, P. (1997). Thrust geometry controlled by

434   erosion and sedimentation: A view from analogue models. *Geology*, *25*(5), 427–430.

435   Mulugeta, G., & Koyi, H. (1992). Episodic accretion and strain partitioning in a model sand wedge. *Tectonophysics*,

436   *202*(2), 319–333.

437   Nakanishi, A., Takahashi, N., Yamamoto, Y., Takahashi, T., Citak, S. O., Nakamura, T., et al. (2018). Three-

438   dimensional plate geometry and P-wave velocity models of the subduction zone in SW Japan: Implications for

439   seismogenesis. *Geology and Tectonics of Subduction Zones: A Tribute to Gaku Kimura: Geological Society of America*

440   *Special Paper*, *534*, 69–86.

441   Ohmori, K., Taira, A., Tokuyama, H., Sakaguchi, A., Okamura, M., & Aihara, A. (1997). Paleothermal structure of the

442   Shimanto accretionary prism, Shikoku, Japan: Role of an out-of-sequence thrust. *Geology*, *25*(4), 327–330.

443   Platt, J. P. (1986). Dynamics of orogenic wedges and the uplift of high-pressure metamorphic rocks. *GSA Bulletin*,

444   *97*(9), 1037–1053.

445   Platt, J. P. (1993). Exhumation of high-pressure rocks: a review of concepts and processes. *Terra Nova*, *5*(2), 119–133.

446   Quigley, T. M., & Mackenzie, A. S. (1988). The temperatures of oil and gas formation in the sub-surface. *Nature*,

447   *333*(6173), 549–552.

448   Rabinowitz, H. S., Savage, H. M., Polissar, P. J., Rowe, C. D., & Kirkpatrick, J. D. (2020). Earthquake slip surfaces

449   identified by biomarker thermal maturity within the 2011 Tohoku-Oki earthquake fault zone. *Nature Communications*,

450   *11*(1), 533.

451   Ranalli, G. (1995). *Rheology of the Earth*. Springer Science & Business Media.

452   Ruh, J. B. (2017). Effect of fluid pressure distribution on the structural evolution of accretionary wedges. *Terra Nova*,

453   *29*(3), 202–210.

454   Ruh, J. B. (2020a). Numerical modeling of tectonic underplating in accretionary wedge systems. *Geosphere*, *16*(6),

455   1385–1407.

456   Ruh, J. B. (2020b). Numerical modelling of tectonic underplating in accretionary wedges (p. 5607).

457   Sakaguchi, A., Yanagihara, A., Ujiie, K., Tanaka, H., & Kameyama, M. (2007). Thermal maturity of a fold–thrust belt

458   based on vitrinite reflectance analysis in the Western Foothills complex, western Taiwan. *Tectonophysics*, *443*(3), 220–

459   232.

460   Sakaguchi, A., Chester, F., Curewitz, D., Fabbri, O., Goldsby, D., Kimura, G., et al. (2011). Seismic slip propagation to

461   the updip end of plate boundary subduction interface faults: Vitrinite reflectance geothermometry on Integrated Ocean

462   Drilling Program NanTro SEIZE cores. *Geology*. https://doi.org/10.1130/g31642.1

463   Schmoker, J. W., & Gautier, D. L. (1988). Sandstone porosity as a function of thermal maturity. *Geology*, *16*(11),

464   1007–1010.

465   Simpson, G. D. H. (2010). Formation of accretionary prisms influenced by sediment subduction and supplied by

466   sediments from adjacent continents. *Geology*, *38*(2), 131–134.

467   Storti, F., & Mcclay, K. (1995). Influence of syntectonic sedimentation on thrust wedges in analogue models.

468   https://doi.org/10.1130/0091-7613(1995)023<0999

469   Sugihara, T., Kinoshita, M., Araki, E., Kimura, T., Kyo, M., Namba, Y., et al. (2014). Re-evaluation of temperature at

470   the updip limit of locked portion of Nankai megasplay inferred from IODP Site C0002 temperature observatory. *Earth,*

471   *Planets and Space*. https://doi.org/10.1186/1880-5981-66-107

472   Tesei, T., Lacroix, B., & Collettini, C. (2015). Fault strength in thin-skinned tectonic wedges across the smectite-illite

473   transition: Constraints from friction experiments and critical tapers. *Geology*, *43*(10), 923–926.

474   Tissot, B. P., & Welte, D. H. (2013). *Petroleum Formation and Occurrence*. Springer Science & Business Media.

475   Tissot, B. P., Pelet, R., & Ungerer, P. H. (1987). Thermal History of Sedimentary Basins, Maturation Indices, and

476   Kinetics of Oil and Gas Generation. *AAPG Bulletin*, *71*(12), 1445–1466.

477   Tobin, H., Hirose, T., Saffer, D., Toczko, S., Maeda, L., Kubo, Y., et al. (2015). Site C0002. *Proceedings of the IODP*.

478   https://doi.org/10.2204/iodp.proc.348.103.2015

479   Tobin, H. J., & Saffer, D. M. (2009). Elevated fluid pressure and extreme mechanical weakness of a plate boundary

480   thrust, Nankai Trough subduction zone. *Geology*, *37*(8), 679–682.

481   Totten, M. W., & Blatt, H. (1993). Alterations in the non-clay-mineral fraction of pelitic rocks across the diagenetic to

482   low-grade metamorphic transition, Ouachita Mountains, Oklahoma and Arkansas. *Journal of Sedimentary Research*,

483   *63*(5), 899–908.

484   Underwood, M. B., Laughland, M. M., Byrne, T., Hibbard, J. P., & DiTullio, L. (1992). Thermal evolution of the

485   Tertiary Shimanto Belt, Muroto Peninsula, Shikoku, Japan. *The Island Arc*. https://doi.org/10.1111/j.1440-

486   1738.1992.tb00064.x

487   Wang, K., & He, J. (1999). Mechanics of low-stress forearcs: Nankai and Cascadia. *Journal of Geophysical Research,*

488   *[Solid Earth]*, *104*(B7), 15191–15205.

489   Waples, D. W. (1981). *Organic Geochemistry for Exploration Geologists*. Springer Netherlands.

490   Wenk, L., & Huhn, K. (2013). The influence of an embedded viscoelastic–plastic layer on kinematics and mass

491   transport pattern within accretionary wedges. *Tectonophysics*, *608*, 653–666.

492   Willett, S. (1992). Dynamic and kinematic growth and change of a Coulomb wedge. *McClay, K. R.*, 19–31.

493   Willett, S., Beaumont, C., & Fullsack, P. (1993). Mechanical model for the tectonics of doubly vergent compressional

494   orogens. *Geology*. https://doi.org/10.1130/0091-7613(1993)021<0371:MMFTTO>2.3.CO

495   Willett, S. D. (1999). Orogeny and orography: The effects of erosion on the structure of mountain belts. *Journal of*

496   *Geophysical Research*, *104*, 28957.

497   Yamamoto, Y., Hamada, Y., Kamiya, N., Ojima, T., Chiyonobu, S., & Saito, S. (2017). Geothermal structure of the

498   Miura–Boso plate subduction margin, central Japan. *Tectonophysics*, *710-711*, 81–87.

499

500

501

502

503

504

505

506

507   **List of Tables**
508   *Table 1: Properties for the different materials used for the model runs*

Rock Type	Density (kg/m^3)	Cohesion (MPa)	Coefficient of friction(μ)	Thermal Conductivity (W/(m K))	Flow law	E (kJ/mol)	n
Water	1000	0	0	20		0	0
Air (Sticky-air)	0	0	0	20		0	0
Décollement	2600	0.001	0.03 /0.08	(1.5+807/(T+77))* (1-exp(-Z^2/1.3e7))	Wet quartzite	154	2.3
Sediments1	2600	0.5/0.05*	4.64/0.2*	(0.96+807/(T+77))* (1-exp(-Z^2/1.3e7))	Wet quartzite	154	2.3

Sediments2	2600	0.5/0.05[*]	4.64/0.2[*]	$(0.96+807/(T+77))*(1-\exp(-Z^2/1.3e7))$	Wet quartzite	154	2.3
Upper Continental Crust	2700	1	0.6	$0.64+807/(T+77)$	Wet quartzite	300	2.3
Lower Continental Crust	2800	1	0.6	$0.64+807/(T+77)$	Wet quartzite	300	3.2
Upper Oceanic Crust	3000	1	0.6	$1.18+474/(T+77)$	Plagioclase An75	300	2.3
Lower Oceanic Crust	3000	1	0.6	$1.18+474/(T+77)$	Plagioclase An75	300	3.2
Mantle Lithosphere	3300	1	0.6	$0.73+1293/(T+77)$	Dry olivine	532	3.5
Asthenosphere	3300	1	0.6	$0.73+1293/(T+77)$	Dry olivine	532	3.5

*Strain-softened Cohesion/Coefficient of friction
T is Temperature, Z is the depth from the seafloor.

509

510

511   *Table 2: Model runs and their specific characteristic observations*

Models	φ_b	φ / φ_{ss}	SR	L	α	D	$<R_o\%>$	$\%_{top-half}$	$\%_{Bottom-half}$
M_0^2	2°	30°/15°	None	123.2±15.7	4.3±0.3°	15.5±7.0	0.54	0.0	12.7
M_0^7	7°	30°/15°	None	97.7±9.9	6.5±0.5°	12.1±3.6	0.60	0.0	22.5
M_0^{12}	12°	30°/15°	None	77.8±4.8	8.9±0.5°	8.7±2.1	0.67	0.0	31.3
$M_{0.1}^{12}$	12°	30°/15°	0.1	76.1±5.9	8.9±0.9°	7.3±1.1	0.71	0.1	35.3
$M_{0.3}^{12}$	12°	30°/15°	0.3	79.3±8.2	8.6±1.3°	7.8±2.5	0.69	0.1	32.0
$M_{0.5}^{12}$	12°	30°/15°	0.5	79.9±7.4	8.5±0.6°	9.5±4.0	0.71	2.7	34.4
$M_{0.7}^{12}$	12°	30°/15°	0.7	81.3±10.5	8.5±1.0°	9.9±5.0	0.73	4.2	41.5
$M_{0.9}^{12}$	12°	30°/15°	0.9	82.5±11.0	8.8±1.5°	13.8±7.8	0.75	14.6	51.8
M_0^{17}	17°	30°/15°	None	71.6±5.0	10.7±0.8°	8.8±3.3	0.83	1.2	40.6
M_0^{22}	22°	30°/15°	None	62.7±6.0	12.8±1.2°	8.0±1.8	0.94	2.0	54.0

φ_b is décollement Strength (internal angle of friction)
φ Sediment Strength
φ_{ss} Sediment Strength (Strain weakened)/(internal angle of friction)
SR Average Sediment rate (mm/yr)
L Average Length (in km) between ~2.5-7.5Myr
α Average Taper angle α (in degrees) between ~2.5-7.5Myr
D Average Distance between the first and second frontal thrust between ~2.5-7.5Myr(in km)
T Average time a frontal thrust remains active between ~3.5-7.5Myr
$<R_o\%>$ Average vitrinite reflectance of the wedge between ~3.5-7.5 Myr
$\%_{top}$ Proportion of >1 eventual $R_o\%$ *(vitrinite reflectance at 7.5 Myr)* at shallow half of the incoming sediment at 2.5 Myr.
$\%_{bottom}$ Proportion of >1 eventual $R_o\%$ *(vitrinite reflectance at 7.5 Myr)* at deep half of the concoming sediments.
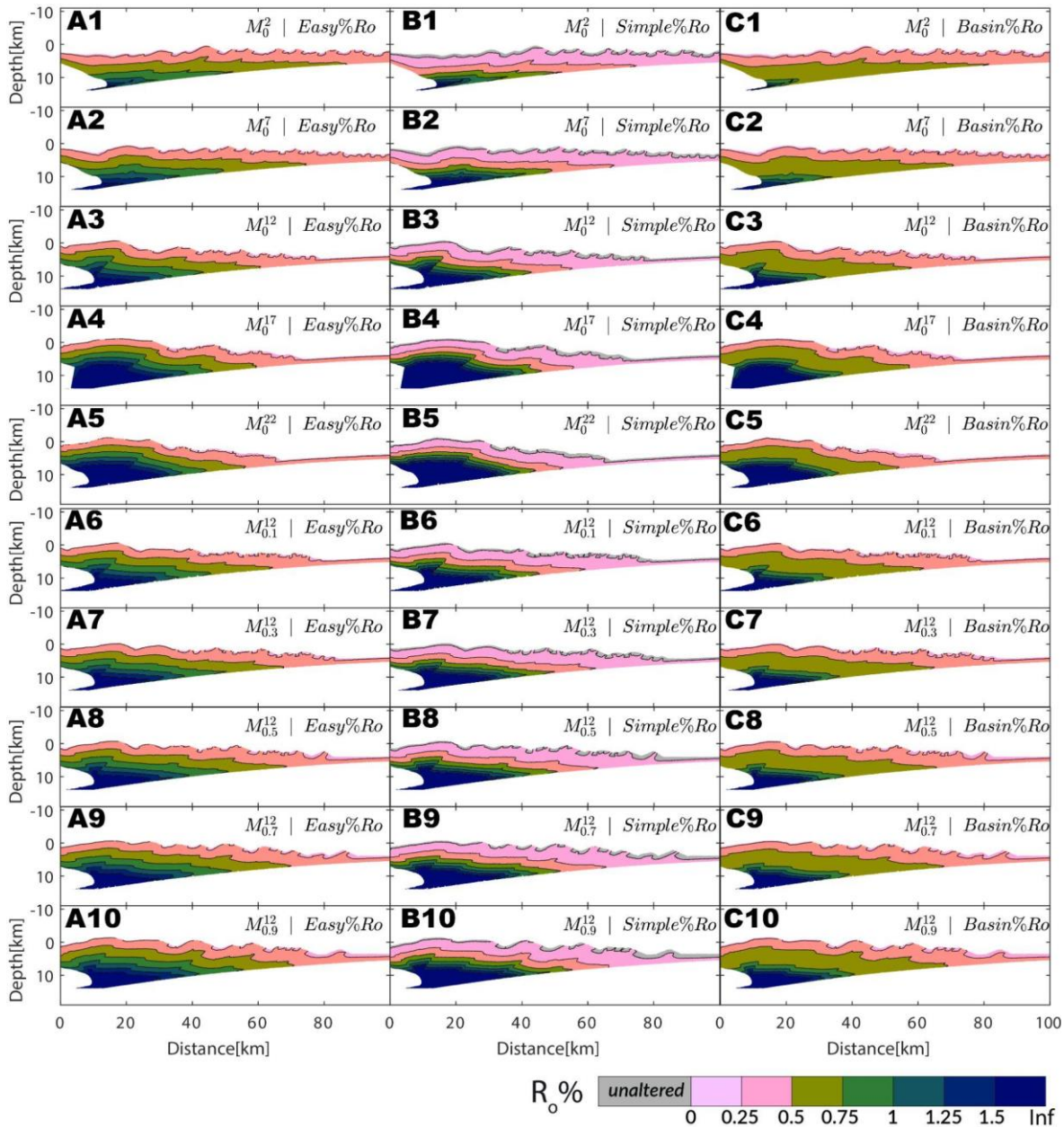
List of Figures

520   ***Fig. 2:*** *The variation of %R₀ for an horizon at the trench depth of each model at 7.5 Myr. Panel A shows all the models with*
521   *different decollement strench (M_0^2-M_0^{22}). Panel B shows all the models with different sedimentation rates ($M_{0.1}^{12}$-$M_{0.9}^{12}$)*
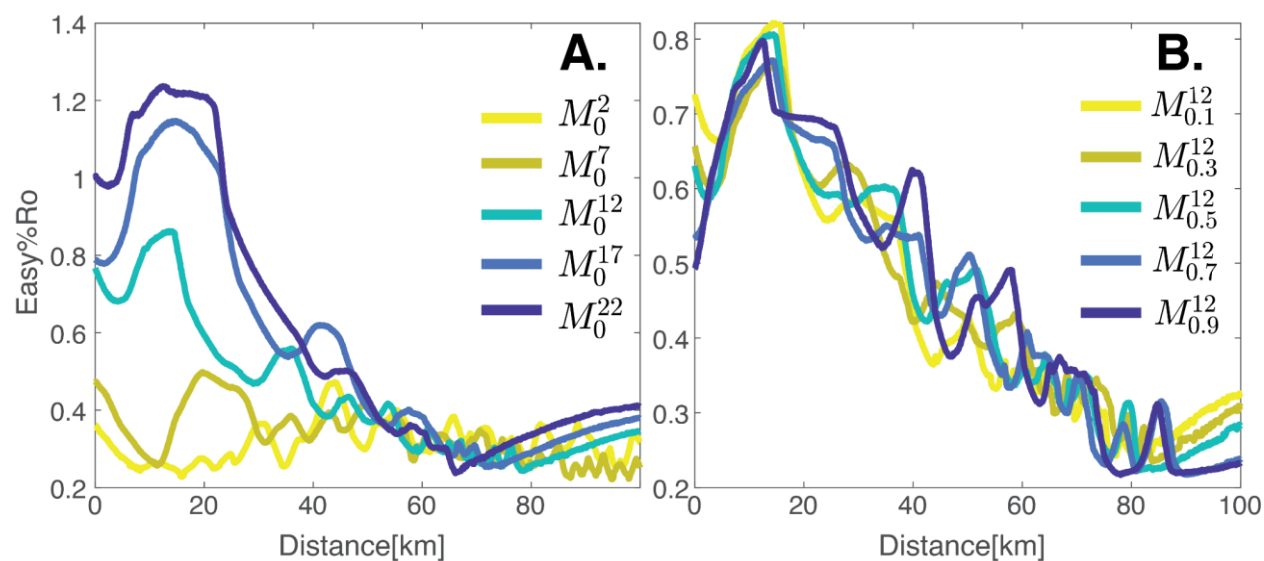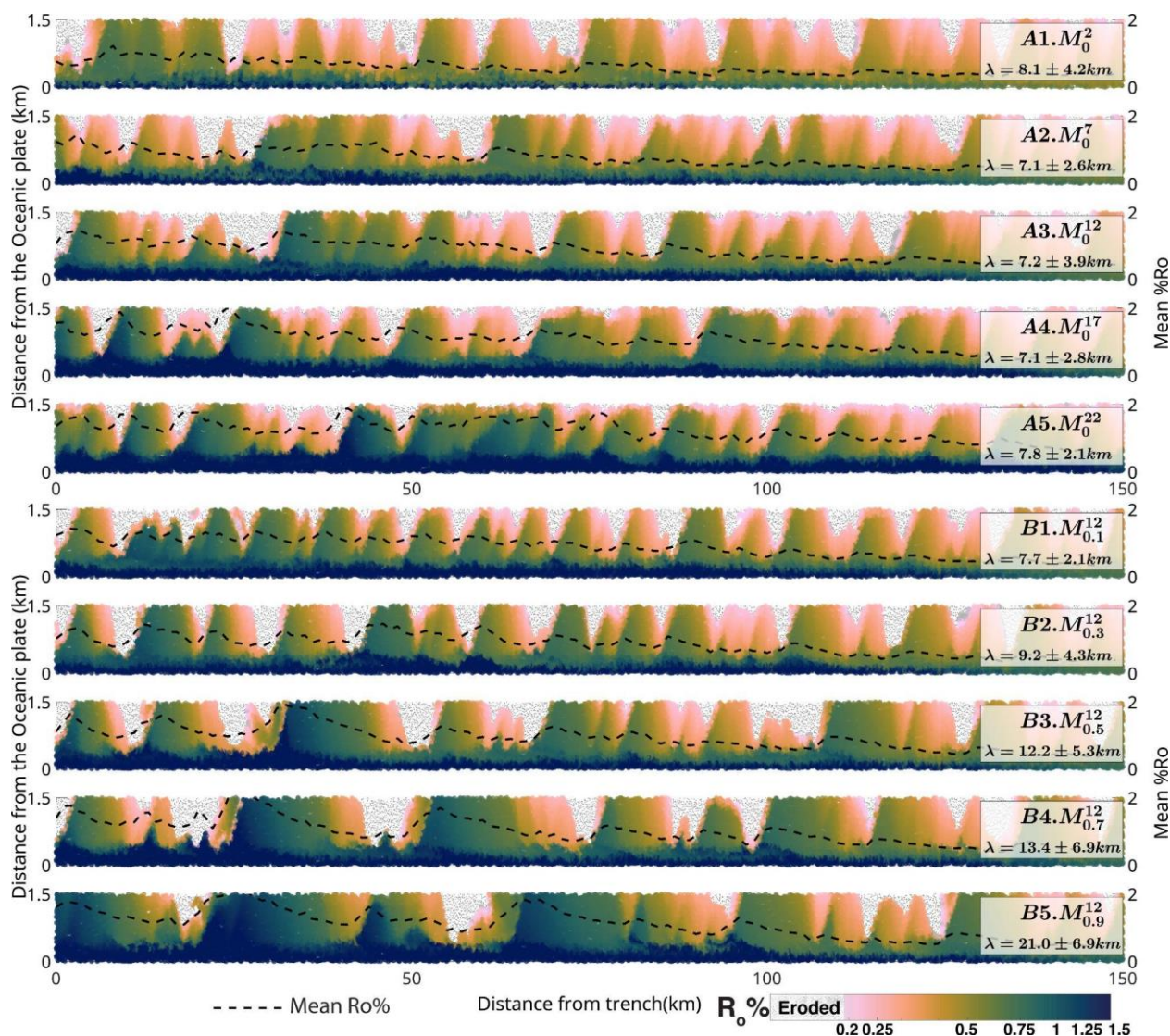

522

Fig. 3: *Map of thermal maturity at 7.5 Myr mapped to sediments at 2.5 Myr. Panel A1-A5,B1-B5 show the mapping for models M_0^2-M_0^{22} and $M_{0.1}^{12}$-$M_{0.9}^{12}$ respectively. The vertical axis (distance from the oceanic plate) has been corrected for the bending of the plate. The horizontal axis represents the distance of sediments from the trench. The grey colour of the markers indicates that these sediments have been eroded/reworked due to slope failure. The broken black line represents the mean %R$_0$ attained sediment at a given distance from the trench. λ represents the horizontal periodicity in mean %R$_0$ for the given model.*

Fig: 4 A. *Vitrinite Reflectance($R_0\%$) vs Maximum Exposure temperature in all models* **B.** *Range of 95% CI for Easy%Ro, Simple%Ro and Basin%Ro*
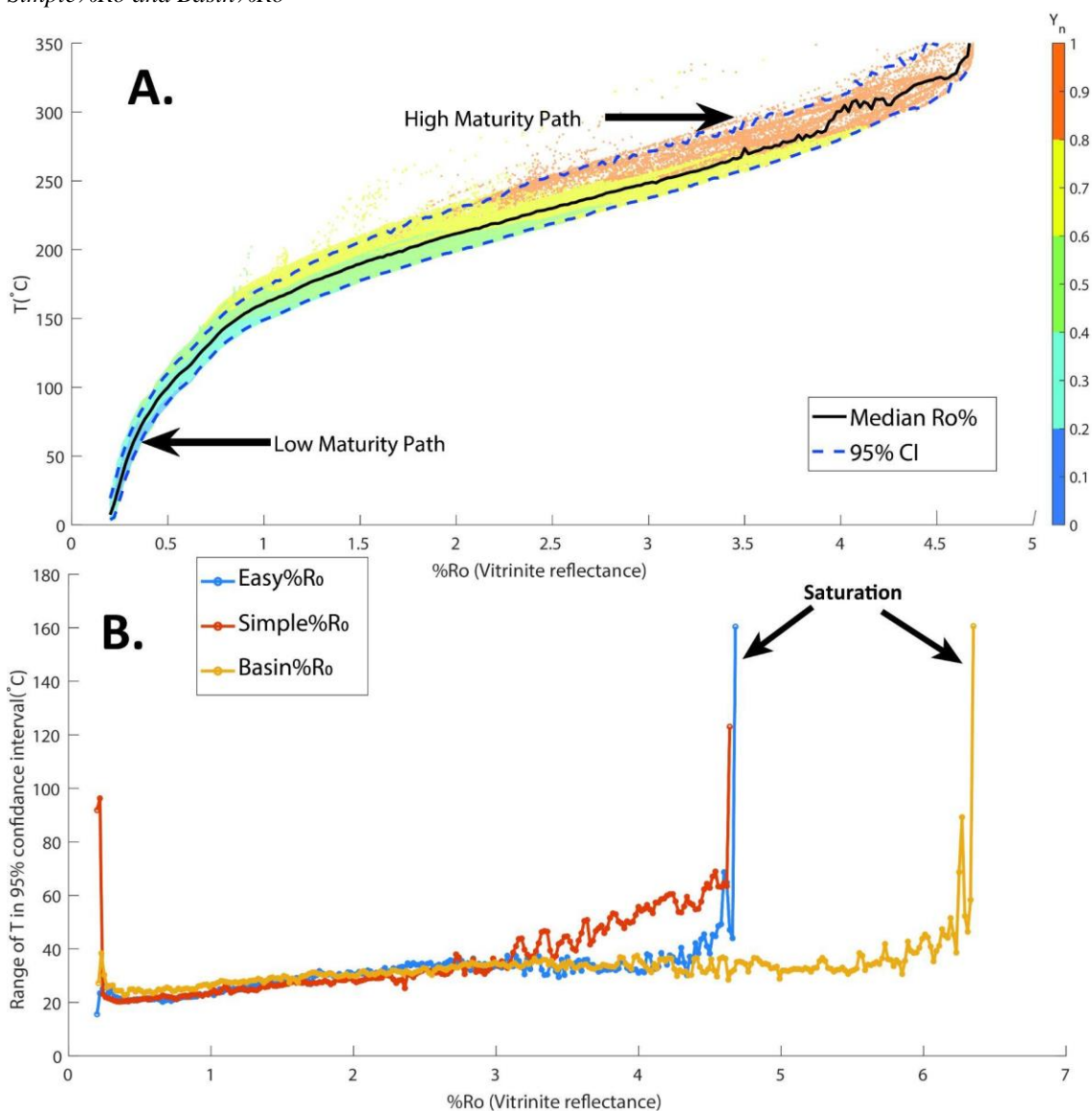
539 **Fig.5:** *Depth vs Thermal maturity(%R₀). The shaded (in voilet) region shows the range of observed R_o%(mean±1SD) from*
540 *the C0002 borehole (Fukuchi et al., 2017), colored lines represent the values in models* M_0^{12}, $M_{0.1}^{12}$, $M_{0.3}^{12}$, $M_{0.5}^{12}$, $M_{0.7}^{12}$, $M_{0.9}^{12}$.
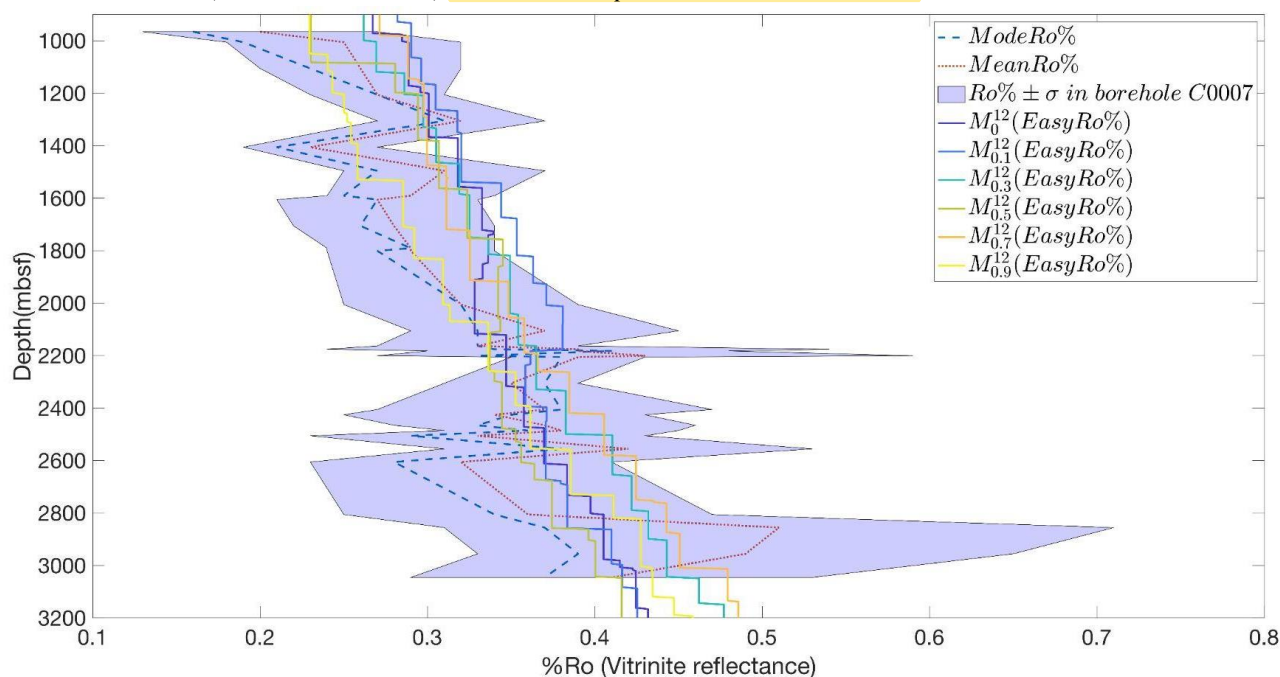

541 .
542
543
544
545
546
547
548
549
550
551
552
553
554
555
556
557
558
559
560
561
562
563
564
565

Fig. 6: *Panel A Mapping of eventual thermal maturity(vitrinite reflectance at 7.5Myr) to a frontal thrust at ~4Myr in model* $M_{0.9}^{12}$*. The lithology of the wedge is shown in panel B. The half arrow represents the active frontal thrust.*
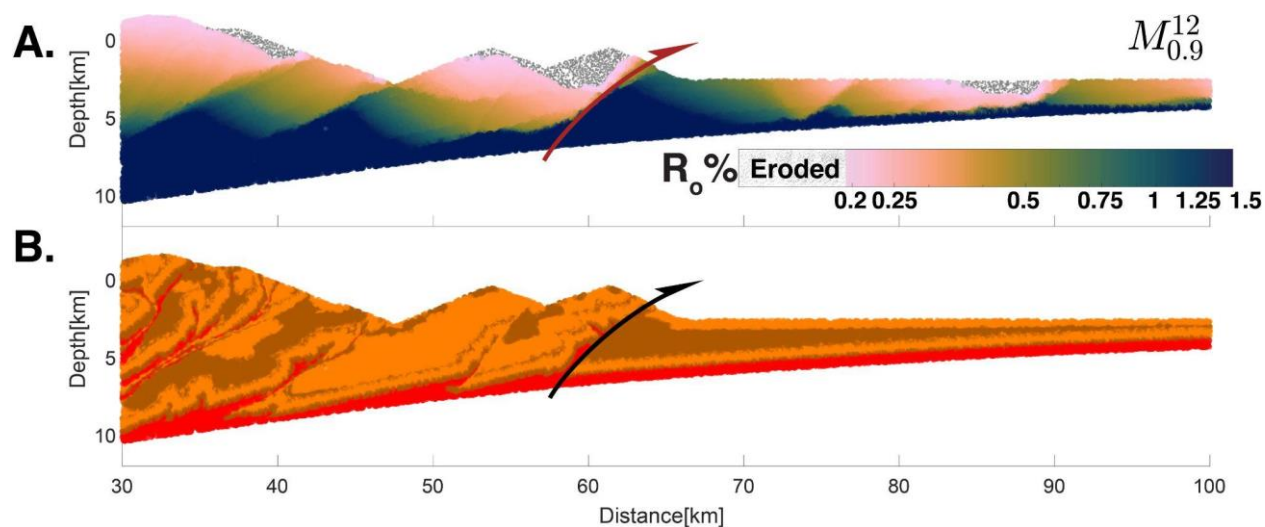
*Fig. 7: Position dependency of thermal maturity preservation. Panel **A**. Model state at ~2.5 Myr with a thermal anomaly placed at 110-125 km from backstop **B**. Model state at ~2.5 Myr with a thermal anomaly placed at 140-155 km from the backstop. **C**. Model state at ~7.5 Myr.*